Available online at www.eccomasproceedia.org
Eccomas Proceedia COMPDYN (2025) 5094-5108

ECCOMAS
Proceedia

COMPDYN 2025
10th ECCOMAS Thematic Conference on
Computational Methods in Structural Dynamics and Earthquake Engineering
M. Papadrakakis, M. Fragiadakis (eds.)
Rhodes Island, Greece, 15-18 June 2025

NUMERICAL MODELLING OF CONNECTIONS FOR INSULATED PRECAST CONCRETE WALLS

Alexia Ribeiro[1], Seyedsajjad Hosseini[1], André Furtado[1], Ricardo Carmo[2], Romain Sousa[3], Wanchai Detphan[4], Yllnor Tmava[4], Wit Derkowski[4] and Eduardo Júlio[1]

[1] CERIS - Civil Engineering Research and Innovation for Sustainability - Instituto Superior Técnico (IST) - University of Lisbon
Adress: Avenida Rovisco Pais, 1049-001 - Lisbon, Portugal
[2] CERIS – Instituto Superior de Engenharia de Coimbra, Portugal
[3] Vigobloco SA, CERIS – Universidade de Aveiro, Portugal
[4] Linnaeus University, Sweden
e-mail: a.brandao.ribeiro@gmail.com
e-mail: seyedsajjad.hosseini@tecnico.ulisboa.pt
e-mail: andré.furtado@tecnico.ulisboa.pt
e-mail: carmo@isec.pt
e-mail: romains@vigobloco.pt
e-mail: wd222bi@student.lnu.se
e-mail: yt222dh@student.lnu.se
e-mail: wit.derkowski@lnu.se
e-mail: eduardo.julio@tecnico.ulisboa.pt

Abstract

In the context of increasing demands for energy-efficient buildings, insulated concrete walls have gained significant adoption in construction. While these walls traditionally serve non-structural purposes, growing requirements for seismic resilience have created new opportunities for innovation. Within the R2UTechnologies-Modular Systems project framework, in collaboration with industry partners, this research aims to transform these elements into load-bearing walls with enhanced dissipative properties. In this scenario, the structural performance of vertical connections between panels emerges as a critical factor for system reliability. This study presents a parametric numerical analysis of a novel connection designed for vertical assembly of precast insulated concrete walls. The research employed finite element analysis using ABAQUS software to develop and validate numerical models against the experimental results of three specimens with the same characteristics, two tested under tensile monotonic and one under cyclic loading. Model validation was achieved through careful comparison of force-displacement relationships and damage progression patterns. Following validation, a parametric study was conducted to investigate the influence of key design parameters, including concrete strength, reinforcement diameter and bolt diameter. The findings provide valuable insights for optimizing connection design in precast insulated concrete walls, contributing to the development of more efficient and seismically resistant building systems.

Keywords: *Precast concrete connections, Anchor bolts, FEM, Concrete damage Plasticity*

ISSN:2623-3347 © 2025 The Authors. Published by Eccomas Proceedia.
Peer-review under responsibility of the organizing committee of COMPDYN 2025.
doi: 10.7712/120125.12797.25486

1 INTRODUCTION

Precast concrete structures have gained significant popularity in modern construction due to their efficiency, quality control, and rapid assembly [1,2]. On these structures, the ability of the connections to dissipate energy and accommodate large deformations without premature failure is essential for ensuring their resilience during earthquakes and has been researched in the last years [3,4]. However, the performance of connections in these structures remains a critical and challenging aspect, particularly when both disassembly and seismic loading are under consideration [5,6]. In this context, the analysis of precast wall connections plays a key role in understanding failure mechanisms and optimizing design parameters to improve environmental and seismic performance.

As part of the *R2U Technologies – Modular Systems* project, an innovative solution is being developed in which thermally insulated precast walls, previously used only as non-structural elements, now serve as structural components in buildings (Figure 1a) to be constructed by the industrial partner *VigoBloco®*. These walls are connected at both ends using anchor bolts, creating a dry connection that facilitates demountability and reuse, thereby enhancing the life-cycle performance of the system [7]. In this structural configuration, lateral loads are resisted by a force pair at the base of the wall, with one side in compression and the other in tension (Figure 1b).

This study focuses on the connection detailing for this insulated load-bearing precast concrete wall system. A representative section of the wall was fabricated and experimentally tested under tensile loading conditions (Figure 1c) to evaluate its behavior and failure mechanisms. To further understand its structural response and explore potential design improvements, a finite element model was developed and validated against experimental results, varying key parameters such as concrete strength, anchor bolt diameter, and rebar diameter. Given the cyclic nature of seismic forces, particular attention was given to failure modes and their implications for seismic performance, ensuring that the connection detailing enhances both strength and ductility while preventing brittle failure mechanisms.

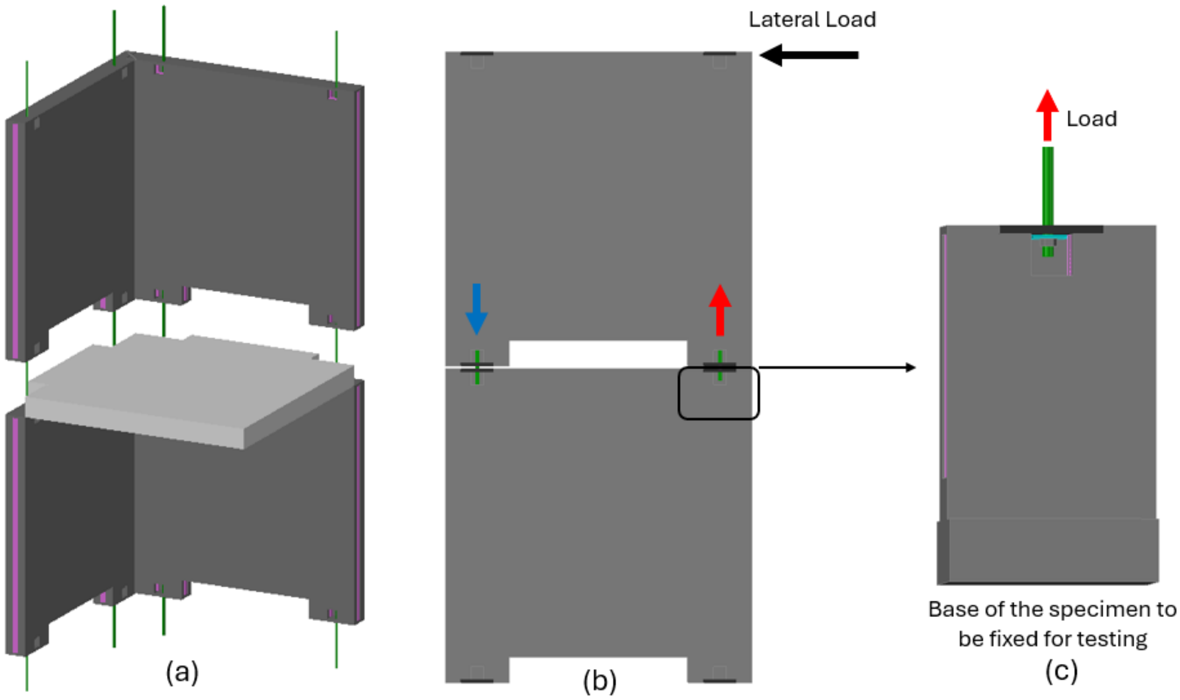

Figure 1: Proposed structural system: (a) general schematic layout (b) Wall to wall connection (c) Representative section of the wall for testing connection detailing

2 METHODOLOGY

2.1 Geometry of the test specimen

From the reference structural system, smaller-scale wall specimens were designed to study the connection behavior at a local level (Figure 1c). Each specimen has a total height of 0.70 m, a width of 0.50 m, and a thickness of 0.22 m, divided into two concrete layers of 0.08m and an EPS insulation of 0.06m. Additionally, each specimen includes a foundation part with a height of 0.15m, thickness of 0.40 m with the same wall width, designed to secure the connection in place during testing.

The concrete layers such in the precast walls were reinforced with a $\phi5/200$ mm mesh near both faces of the concrete layers. On the small foundation C-shaped and L-shaped rebars were positioned to reinforce this region making sure there is no failure in this region, since it is not the region of interest.

To make the connection it was used one 0.22m x 0.25m steel plate with four welded steel rebars, this steel rebars are also embedded into the concrete. On the connection region one additional O-shaped steel rebar was positioned around the four welded rebars (see Figure 3).

2.2 Modelling description

To simulate the behavior of the studied connection, a numerical model was developed in Abaqus [8] mating as close as possible the experimental setup. For the boundary condition, the steel profile used to secure the bottom of the specimen to the Instron 600 testing machine was also included in the model. To properly constrain it, a reference point was created at the center of the bottom surface and coupled with the steel apparatus (represented in red in Figure 2). To apply the load, a second reference point was placed at the center of the bolt, where the load was applied under displacement control, mirroring the experimental procedure.

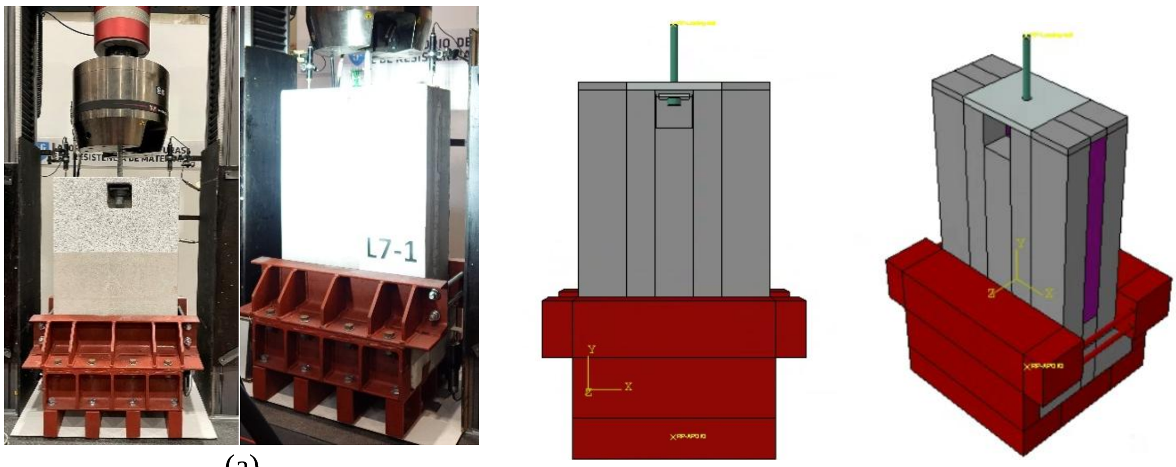

(a) (b)

Figure 2: Modelling strategy (a) Experimental setup (b) Numerical model.

It was defined as a tie connection between the welded rebars and the surrounding concrete and with the steel plate where these bars were welded. The EPS and the concrete part were also connected by a tie pair.

There was defined a surface-to-surface contact standard with a tangential frictional behavior of 0.5 and normal as hard contact to the pairs: specimen foundation to steel support; steel bolt perimeter to the hole surface of the plate and washer; the steel plate to the surrounding concrete; the steel washer to the steel plate and surrounding concrete (see Figure 3).

2.3 Meshing and element types

The numerical model consists of different structural components, each assigned an appropriate element type to balance computational efficiency and accuracy. The L-shaped, C-shaped, and O-shaped steel rebars were modeled using T3D2 elements, which are 2-node linear 3D truss elements. These elements are suitable for modeling slender structural components that primarily resist axial forces. A global mesh size of 5 mm was applied to these elements, and an embedded constraint was used to integrate the rebars within the concrete and EPS (Expanded Polystyrene) parts, ensuring proper force transfer and interaction between materials.

The concrete, EPS, steel plate, washer, steel bolt, steel support, and welded steel rebars were all modeled using C3D4 elements, which are 4-node linear tetrahedral solid elements (Figure 3). This element type was selected due to the complex geometry of the connection, allowing for an accurate representation of the structural components while maintaining reasonable computational costs.

To verify mesh convergence, different meshing strategies were tested. A finer mesh with element sizes reduced by half was considered, as well as a quadratic-element mesh with the same global size but using C3D10 elements, which are 10-node quadratic tetrahedral elements, instead of C3D4. The results showed that while the finer and quadratic element meshes provided slightly improved accuracy in terms of load-displacement behavior and maximum load, the differences were minimal. However, the computational cost increased significantly, with the analysis time rising from 5 hours to over 50 hours in some cases. Given the trade-off between accuracy and computational efficiency, the original linear mesh was considered the most appropriate for the remainder of this study.

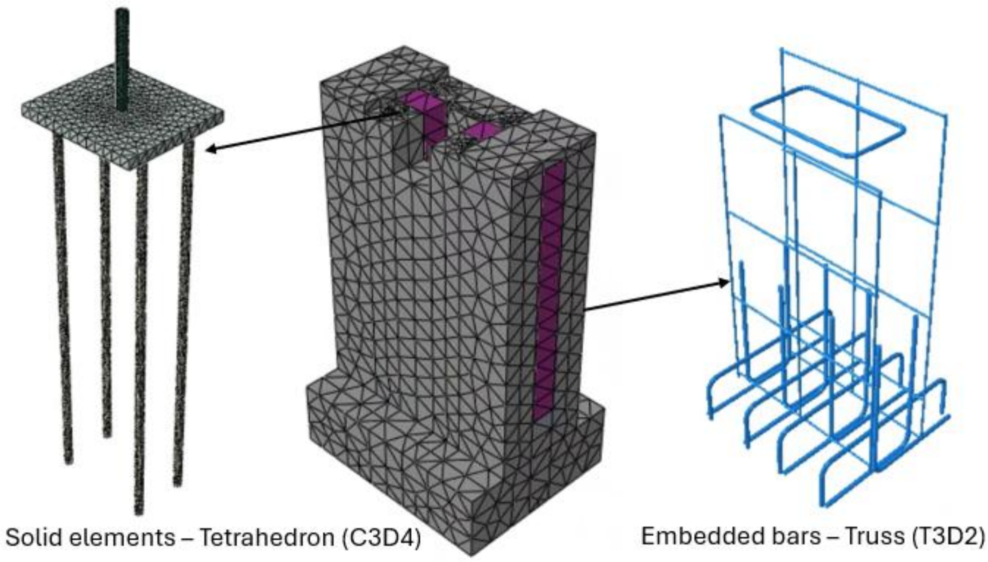

Figure 3: Mesh and element types

2.4 Definition of materials

2.4.1 Concrete

The concrete used in the experimental program is C50/60 class concrete. For C50/60 concrete, for reference, it is specified in Eurocode 2 [9] the characteristic compressive strength is 50 MPa, the tensile strength is 4.1 MPa, and the elastic modulus is 37000 MPa. In the experimental tests from three concrete cubes, the concrete exhibited a mean compressive strength of 60 MPa at 28 days, this mean value will be used for the modeling properties (Table 1) as it goes closer to the experiments.

Property	Equation	Value
Compressive Strength (fcm)	Experimental	60 MPa
Elastic Modulus (E)	4700 * √fcm	36406 MPa
Tensile Strength (ftm)	0.3 * $fcm^{2/3}$	4.6 MPa
ε_0	(2 * fcm) / E	0.0033
Poison		0.15
Dilatation angle		28
Eccentricity		0.1
fb0/fc0		1.16
K		0.67
Viscosity parameter		5.0E-5

Table 1: Concrete properties for concrete damage plasticity model definition

Figure 4 shows the curves defined for the material behavior for compressive and tensile elastic-plastic as well as the damage parameter [10,11].

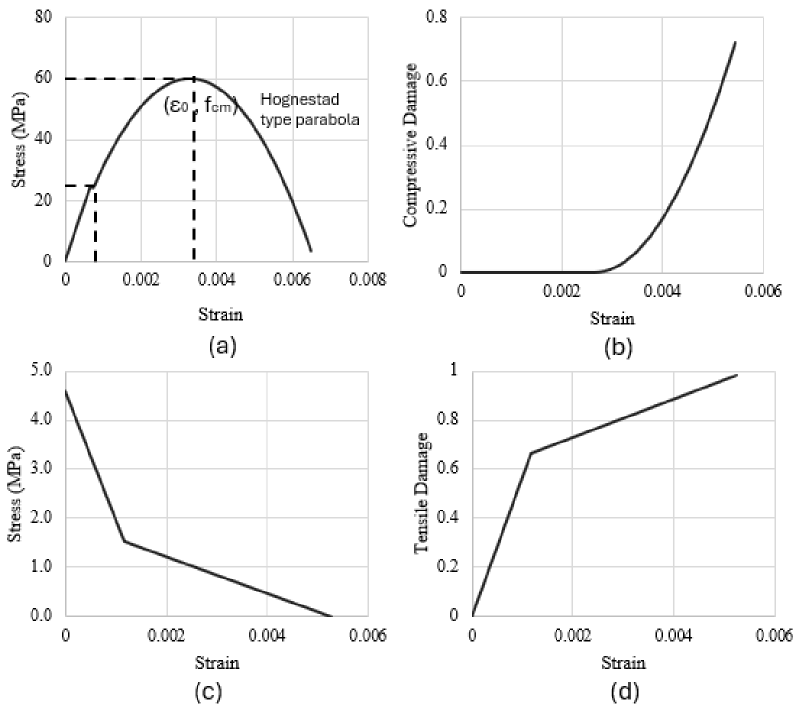

Figure 4: Concrete properties (a) Compressive behavior (b) Compressive damage (c) Tensile behavior (d) Tensile damage

2.4.2 Steel

For the bolt, an M24 8.8-grade threaded steel rod was used. The steel for concrete reinforcement was A500 NR, while S355 steel was used for the steel plate and washer. All steel components were considered to have an elastic modulus of 210 GPa. The strength properties for each steel type are presented in Table 2.

Additionally, tensile tests were conducted on 8.8-grade M24 threaded steel rod (bolt) with an internal diameter of 20.2 mm. The obtained stress-strain curve indicated an average yield strength of approximately 808 MPa, corresponding to the end of the linear segment, and an average maximum stress of approximately 1000 MPa (CoV: 1%) from three specimens.

Property	Class	E (MPa)	fy (MPa)	fu (MPa)
Threaded rod or bolt	8.8	210000	808	1000
Steel plate and washer	S355	210000	310	355
Ribbed bars	A500NR	210000	400	520

Table 2: Steel elements properties

2.4.3 EPS

The EPS is a nonstructural material, it was modeled as an elastic material with elasticity of 3MPa and poison of 0.1.

2.5 Validation of the model

The comparison between the numerical and experimental results is shown in the force-displacement graph (Figure 5). The numerical model (black solid line) exhibits a steeper initial stiffness compared to the experimental curves, suggesting a slightly stiffer response than the actual specimens. This discrepancy can be attributed to the initial accommodation of the testing apparatus.

In the simulation, failure was considered to occur when the time step was reduced below 1E-10 due to material nonlinearities. The peak load predicted by the model (283kN) is slightly higher than the mean experimental maximum force (262 kN) but remains within an acceptable range, considering the standard deviation (SD = 22 kN) and coefficient of variation (CoV = 9%) among the three experimental results. The experimental curves exhibit a more gradual softening and greater dispersion in failure displacements, whereas the numerical model maintains a more idealized, stiffer response. This suggests that certain effects related to material and geometrical variability are not captured in the numerical simulation.

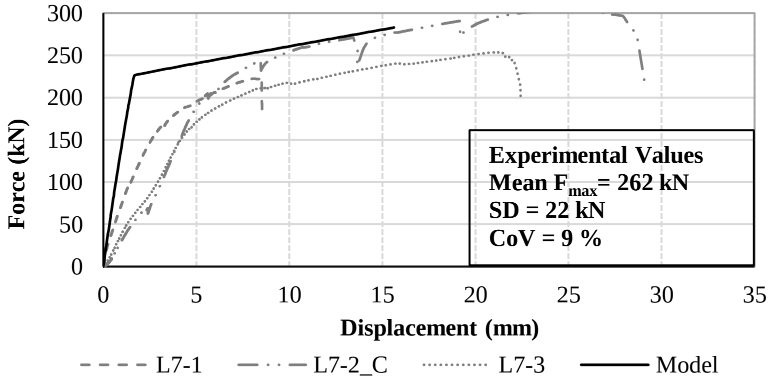

Figure 5: Force - displacement curves comparison.

The numerical model successfully captures the overall trend and failure locations at the front and the back of the specimen, as shown in Figure 6 through the SDEG (Status of Damage Evolution for General Failure) plot. This damage variable quantifies material degradation throughout the simulation, ranging from 0 (undamaged material) to 1 (complete failure).

Despite some limitations, the model provides a good approximation of the experimental response, particularly in terms of peak strength and failure modes. Therefore, it is considered validated and suitable for the parametric variations analyzed in this study. Future improvements will focus on enhancing the accuracy of post-peak behavior by implementing cohesive elements between the steel rebars and concrete, which could better simulate bond-slip effects and the observed variability in stiffness and post-peak behavior.

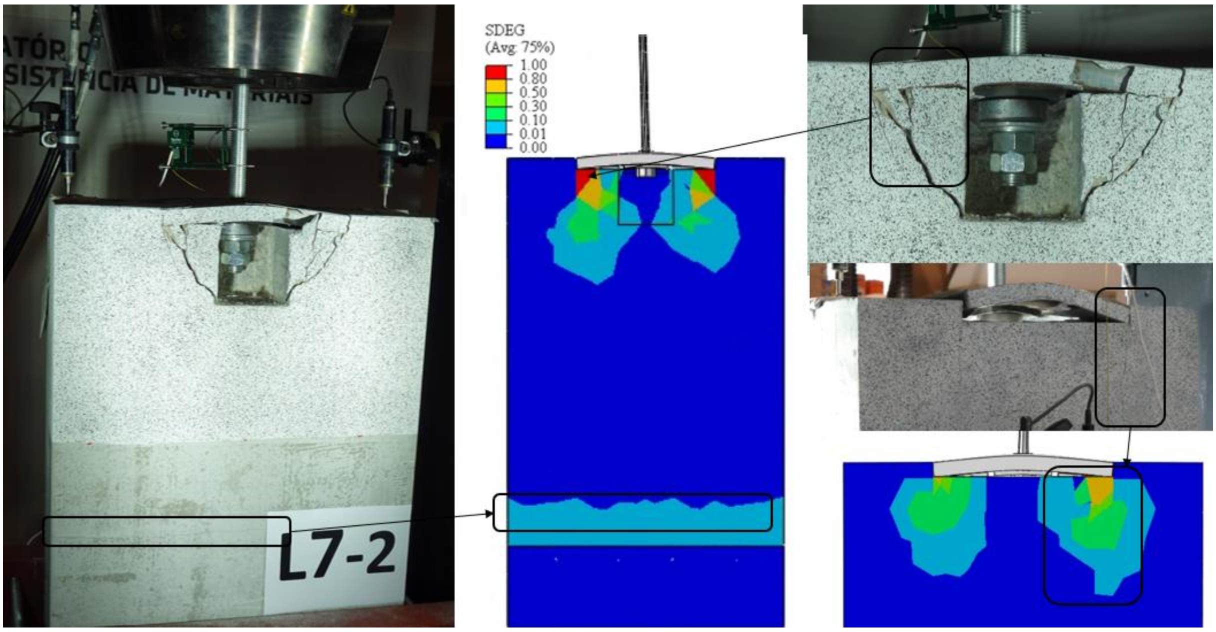

Figure 6: Failure modes comparison between experimental and numerical results

2.6 Description of parametric study

The parametric study aims to evaluate the influence of concrete strength, bolt diameter, and rebar diameter on the structural performance of the connection. The Reference Model corresponds to the calibrated numerical model based on experimental properties, serving as the benchmark for comparison.

2.6.1 Concrete Strength

To assess the effect of concrete strength, three different compressive strengths were considered: 40 MPa, 60 MPa (Reference Model), and 80 MPa. The 60 MPa concrete corresponds to the experimental reference, while the 40 MPa and 80 MPa variations were introduced to evaluate how a weaker or stronger concrete affects the connection’s behavior. Since concrete strength directly influences its plasticity and failure mechanisms, the elastic modulus and plasticity parameters were adjusted accordingly (Figure 7), following the considerations explained in Section 2.3.1. The objective of this variation is to analyze how different levels of concrete strength impact stiffness, failure mode, and overall load-bearing capacity of the connection.

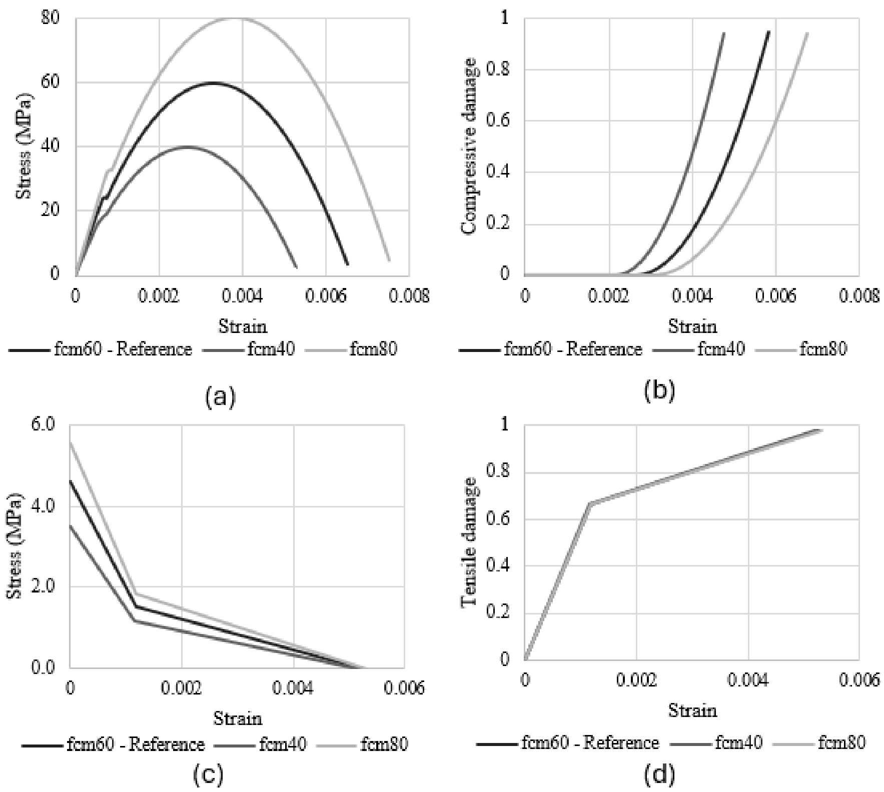

Figure 7: Concrete properties for the three different strengths studied (a) Compressive behavior (b) Compressive damage (c) Tensile behavior (d) Tensile damage

2.6.2 Bolt Diameter

The second parameter investigated is the diameter of the anchor bolts used in the connection. The reference model employs M24 bolts, but additional simulations were conducted with M22 and M27 bolts to assess how changing the bolt size influences the force transfer mechanism and stress distribution within the connection. Smaller-diameter bolts, such as M22, may lead to increased stress concentrations and potentially affect failure modes, whereas larger-diameter bolts, such as M27, could enhance load-bearing capacity but might also alter the stress distribution between the concrete and steel components. The analysis will help determine the optimal bolt size for balancing strength, stiffness, and failure behavior.

2.6.3 Rebar Diameter

Lastly, the effect of the rebar diameter on the connection's performance was investigated. The reference model uses 16 mm diameter rebars, while additional simulations were conducted using 12 mm and 20 mm rebars. Reducing the rebar diameter to 12 mm could lead to reduced reinforcement stiffness and lower load capacity, potentially increasing concrete damage due to a weaker confinement effect. Conversely, increasing the rebar diameter to 20 mm might improve the connection’s strength and stiffness, though it could also affect failure modes and crack propagation patterns. This variation aims to provide insights into the interaction between reinforcement and concrete in the connection and how different rebar sizes influence the structural response.

3 RESULTS AND DISCUSSION

3.1 Concrete strength

The analysis of different concrete strengths (40 MPa, 60 MPa, and 80 MPa) shows that the maximum load capacity of the connection is not significantly affected by this variation (Figure 8). The initial response of all three models is nearly identical, indicating that the initial stiffness of the connection remains largely unchanged with different concrete strengths. Additionally, the peak force values are very similar across the models, suggesting that concrete strength has a limited impact on the ultimate load capacity. However, the failure displacement varies slightly (marked with the x in Figure 8), indicating that the ductility of the connection may be influenced by the type of concrete used.

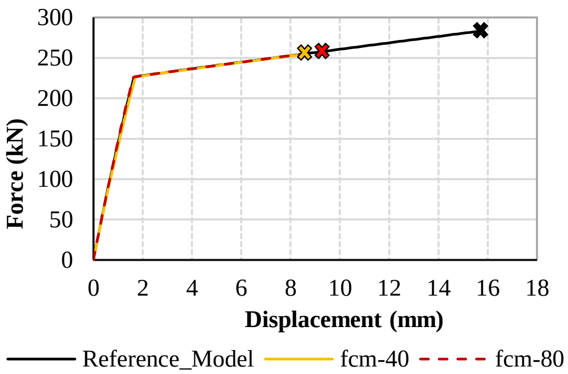

Figure 8: Force-displacement response for different concrete strengths.

The damage distribution in the concrete (Figure 9) shows that, for the 40 MPa model, the damaged area extends further (276 mm), meaning that the weaker concrete results in a wider spread of cracks. In the 60 MPa reference model, this zone is smaller (230 mm), representing intermediate behavior. For the 80 MPa concrete, the damage region is the smallest (198 mm), suggesting that failure occurs in a more localized manner, possibly due to the reduced deformation capacity before rupture. This behavior indicates that higher-strength concrete can lead to a more brittle response, concentrating stresses in smaller regions.

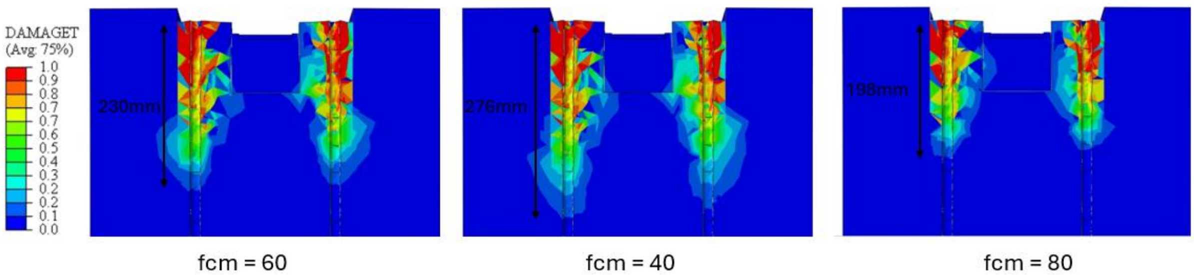

Figure 9: Concrete tensile damage distribution for different concrete strengths.

The stress distribution in the reinforcing bars (Figure 10) reveals that the maximum stresses reach similar values across all models (σ _max ≈ 412-416 MPa), indicating that variations in concrete strength do not significantly affect the stresses in the reinforcement. However, in the experimental tests, failure ultimately occurs due to the failure of one of the rebars, despite the presence of tensile damage in the concrete. This behavior is also observed in the simulation, where the stresses in the steel bars approach their yield limit, confirming that failure primarily occurs in the steel, but is influenced by accumulated damage in the concrete.

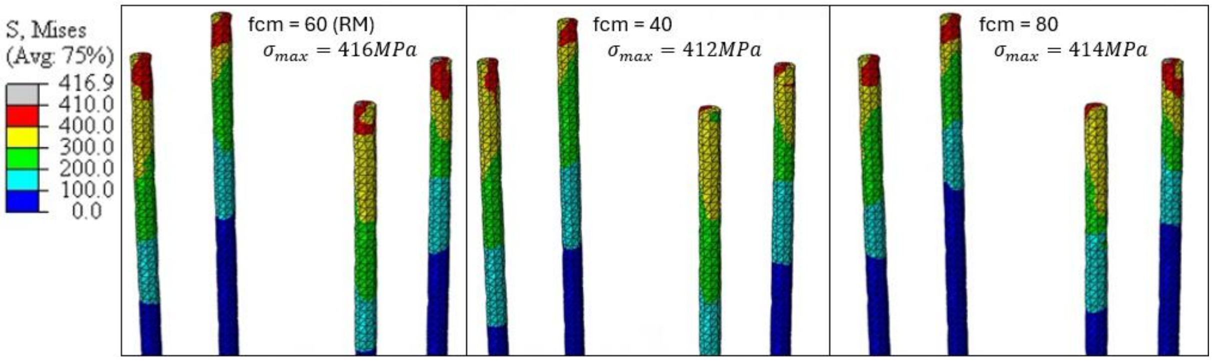

Figure 10: Von Mises stress distribution in the rebars for different concrete strengths.

The initial stiffness of all three models appears nearly identical, meaning that the variation in concrete strength does not significantly affect the elastic response of the connection (as shown in Figure 8). However, differences emerge in the post-peak behavior. The 60 MPa model sustains more deformation before numerical instability occurs, followed by the 80 MPa, and then the 40 MPa model, which fails with the least displacement. This aligns with the stress distribution in the anchor bolts (Figure 11), where the 60 MPa model exhibits the highest stress concentration, followed by the 80 MPa and the 40 MPa.

This suggests that the dominant factor influencing failure is the deformation capacity of the anchor bolts. In the 60 MPa model, the combination of moderate concrete strength and sufficient deformability allows the bolts to develop higher stresses before failure. In contrast, in the 80 MPa model, the stiffer concrete restricts deformation slightly, lowering bolt stress. The 40 MPa model, being more flexible, leads to a more distributed load transfer, but fails at a lower displacement. Thus, while stiffness remains largely unchanged, the deformation capacity are influenced by the interaction between concrete strength and anchor bolt behavior.

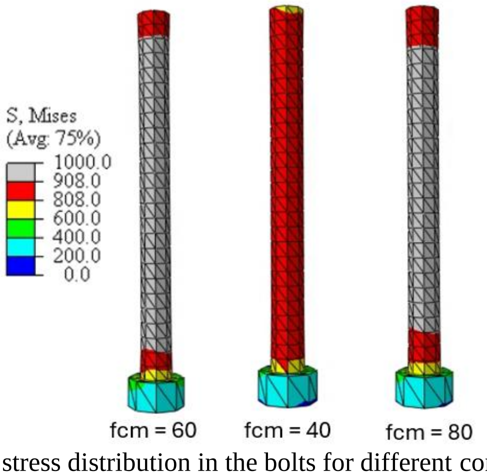

Figure 11: Von Mises stress distribution in the bolts for different concrete strengths.

3.2 Bolt diameter

The force-displacement graph (Figure 12) indicates that varying the bolt diameter has little effect on the stiffness of the connection, as the initial slopes of all curves remain similar. However, differences are observed in the peak load and displacement at failure. The M22 bolt exhibits the lowest ultimate strength, while the M27 bolt achieves the highest, with the reference model (M24) in between. This suggests that increasing the bolt diameter enhances the load capacity of the connection, although it may also affect the deformation behavior.

Notably, the M22 and M24 configurations exhibit a pronounced yield plateau, indicating significant inelastic deformation before failure. In contrast, the M27 configuration lacks this yield plateau, suggesting a more brittle failure mode. This observation is further supported by Figure 15, which shows that the connection with the M27 bolt does not reach the yield stress. This explains the brittle failure observed in the force-displacement response in Figure 12.

These results highlight an important trade-off in bolt sizing: while larger bolts increase strength, they may also lead to more brittle failure modes, reducing the ductility and energy dissipation capacity of the connection. This aspect is particularly relevant for seismic applications, where ductility and controlled energy dissipation are critical to ensuring structural resilience.

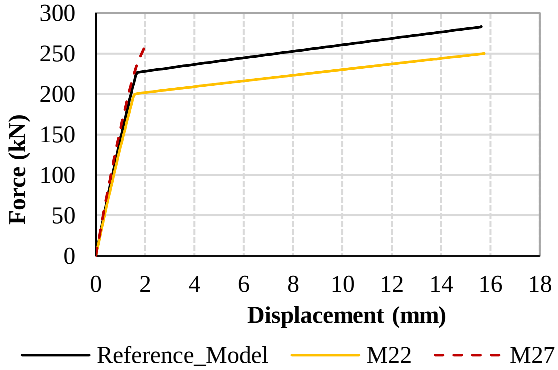

Figure 12: Force-displacement response for different bolt diameters.

The damage plots (Figure 13) reveal that the M22 configuration experiences the smaller concrete damage, with a failure region extending up to 187 mm. The M27 bolt shows a slightly smaller damage area (212 mm), whereas the M24 reference model presents the largest extent of damage (230 mm). These results suggest that increasing the bolt size may improve strength but does not necessarily mitigate concrete damage, as stress concentrations shift rather than decrease.

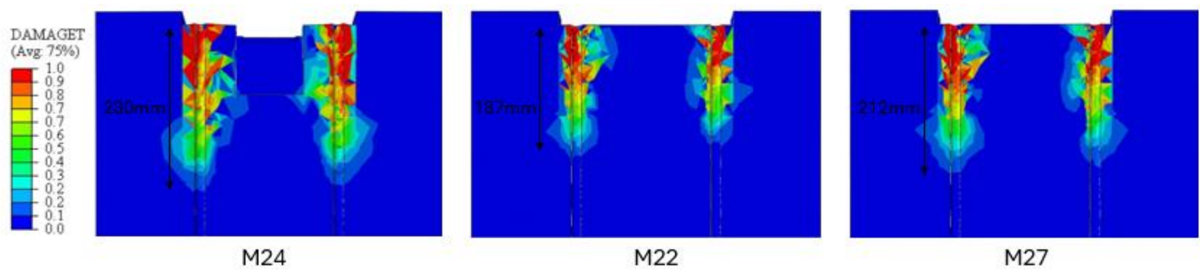

Figure 13: Concrete tensile damage distribution for different bolt diameters.

Figure 14 presents the stress distribution in the rebars, demonstrating that increasing the bolt diameter has little effect on the maximum stress in these elements. The highest stress values are similar across all configurations, with slightly higher stresses in the M27 case (418 MPa) compared to the reference model (416 MPa) and the M22 configuration (412 MPa). This suggests that bolt size variation does not significantly alter the force transfer mechanism to the rebars. However, it influences the relative timing of this transfer in relation to bolt yielding, allowing more or less time for the bolts to yield. Ultimately, the rebars yielding remains a critical factor in determining the maximum force and displacement each specimen can sustain before losing convergence.

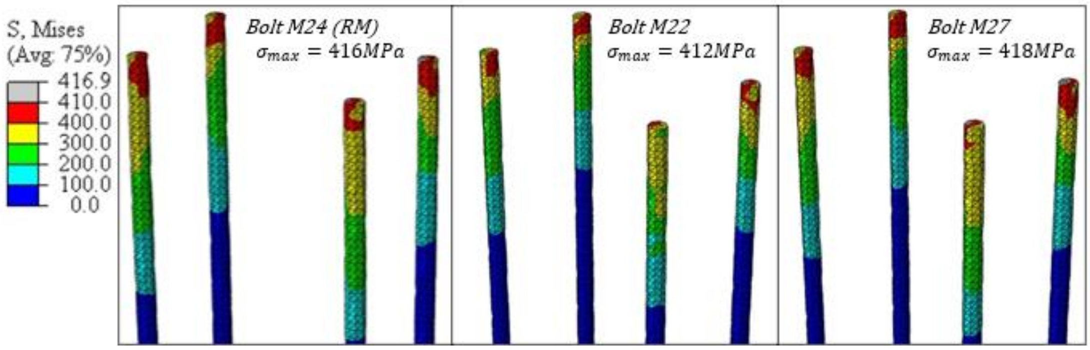

Figure 14: Von Mises stress distribution in the rebars for different bolt diameters.

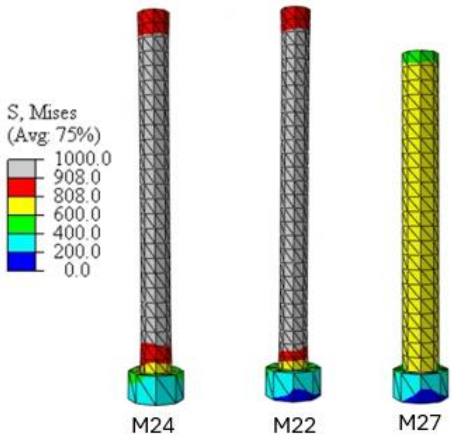

Figure 15: Von Mises stress distribution in the bolts for different bolt diameters.

3.3 Rebar diameter

Based on Figures 16 to 19, the impact of rebar diameter variation on the structural response of the connection can be observed. Figure 16 indicates that the initial stiffness of the connections is not strongly affected by the rebar diameter. However, differences arise in ultimate strength and post-yielding behavior. The connection with 12 mm rebar exhibits the lowest ultimate strength, with a more brittle failure behavior, whereas the 20 mm rebar performs similarly to the reference model (16 mm) but with a more pronounced yielding plateau.

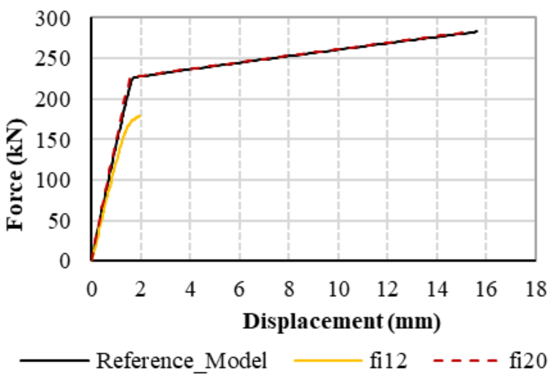

Figure 16: Force-displacement response for different rebar diameters.

Figure 17 shows that the connection with 12 mm rebar has the shortest concrete damage length (130 mm), while the 20 mm rebar reaches 195 mm, positioning itself between the ϕ12 and the reference model (230 mm). However, despite the smaller damage length, the severity of concrete damage is higher for ϕ12. This suggests that thinner rebars tend to limit the propagation of concrete damage, whereas thicker rebars may increase the extent of damage, requiring a longer anchorage length. Moreover, Figure 18 reveals that the rebars in the ϕ12 connection experience more severe yielding compared to ϕ16 and ϕ20, which justifies the limited plastic deformation observed in Figure 16 and the premature failure of the connection.

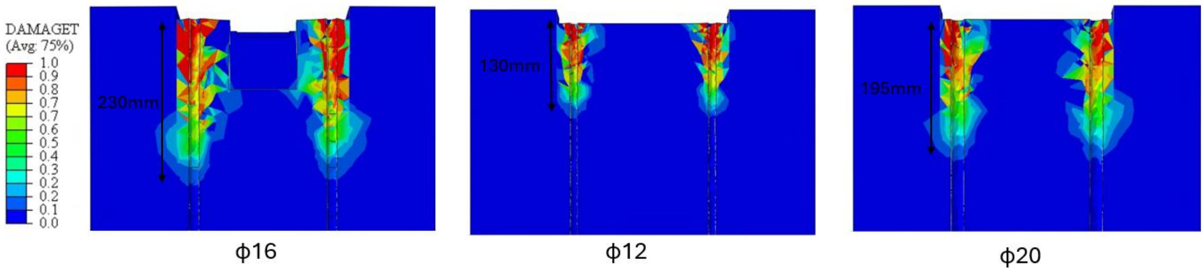

Figure 17: Concrete tensile damage distribution for different rebar diameters.

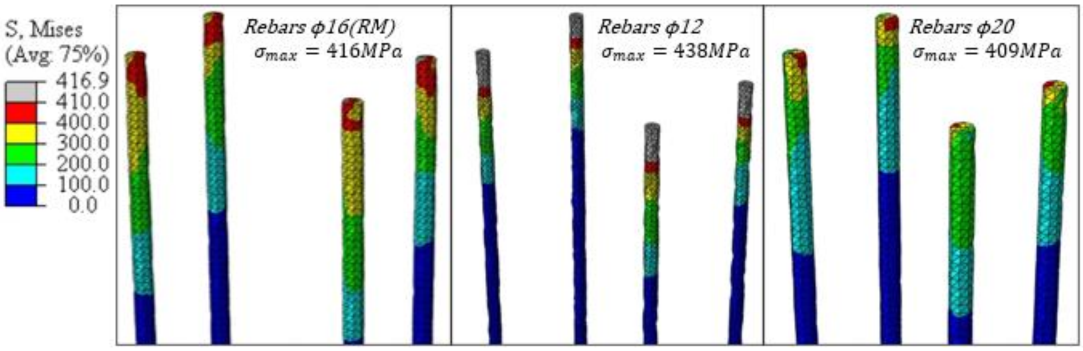

Figure 18: Von Mises stress distribution in the rebars for different rebar diameters.

Finally, Figure 19 shows that in ϕ16 (reference model) and ϕ20 connections, the bolts reach high stress levels, exceeding 908 MPa. This indicates that these elements have yielded, explaining the plateau observed in Figure 16. In contrast, the ϕ12 connection exhibits bolt stresses ranging from 600 to 808 MPa, meaning the bolts did not reach the yielding point.

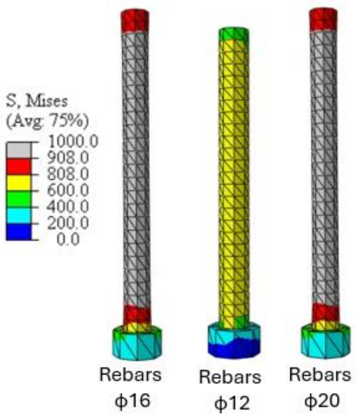

Figure 19: Von Mises stress distribution in the bolts for different rebar diameters.

4 CONCLUSIONS AND FUTURE WORK

This study investigated the structural behavior of a bolted connection system for insulated load-bearing precast concrete walls through numerical analysis, considering variations in bolt diameter, rebar diameter, and concrete strength. The results indicate that variations in concrete strength have a minimal influence on the overall structural performance of the connection. Peak force values remain similar across all models, suggesting that concrete strength has a limited impact on the ultimate load capacity. However, failure displacement varies slightly, with higher-strength concrete reducing deformation capacity, though not significantly.

Increasing the bolt diameter enhances the load capacity of the connection; however, it does not necessarily lead to improved ductility. This is evident in the M27 case, which exhibited a more brittle failure mode. The rebar diameter also plays a crucial role in defining the post-yielding behavior and overall failure mechanism. Smaller rebars, such as the 12 mm case, exhibited more severe yielding and premature brittle failure, whereas larger rebars, such as the 20 mm case, performed similarly to the 16 mm bars.

In conclusion, the force-displacement behavior suggests that an optimal combination of bolt and rebar sizes is essential to balance strength and ductility. While increasing the bolt size can enhance the load-bearing capacity, the rebar must be proportionally adjusted to prevent premature and brittle failure. Future numerical work will focus on improving the representation of the bond interaction between the rebar and concrete, as experimental results indicate that the rebars undergo significantly greater deformation, including necking and eventual failure. In contrast, the numerical model constrains this behavior due to the surrounding concrete and tie connections used. Refining this aspect will enhance the accuracy of the simulations and provide a more realistic prediction of failure mechanisms, contributing to the optimization of connection detailing in precast concrete structures.

5 ACKNOWLEDGMENTS

The authors acknowledge the support of Fundação para a Ciência e Tecnologia (FCT) which finances the authors' research centre, CERIS—Civil Engineering Research and Innovation for Sustainability with the funding reference UIDB/04625/2020. This article is a result of the Innovation Pact "R2UTechnologies|modular systems" (C644876810-00000019) by "R2UTechnologies" Consortium, co-financed by NextGeneration EU, through the Incentive System "Agendas para a Inovação Empresarial" ("Agendas for Business Innovation"), within the Recovery and Resilience Plan (PRR).

REFERENCES

[1] R. Martins, R. do Carmo, H. Costa, E. Júlio, A review on precast structural concrete walls and connections, Advances in Structural Engineering 26 (2023) 2600–2620. https://doi.org/10.1177/13694332231191073.

[2] Y.C. Kurama, S. Sritharan, R.B. Fleischman, J.I. Restrepo, R.S. Henry, N.M. Cleland, S.K. Ghosh, P. Bonelli, Seismic-Resistant Precast Concrete Structures: State of the Art, Journal of Structural Engineering 144 (2018). https://doi.org/10.1061/(ASCE)ST.1943-541X.0001972.

[3] F. Zhao, F. Xiong, G. Cai, H. Yan, Y. Liu, A. Si Larbi, Performance and numerical modelling of full-scale demountable bolted PC wall panels subjected to cyclic loading, Journal of Building Engineering 63 (2023) 105556. https://doi.org/10.1016/j.jobe.2022.105556.
[4] B. Zhao, D. Wu, H. Zhu, New modular precast composite shear wall structural system and experimental study on its seismic performance, Eng Struct 264 (2022) 114381. https://doi.org/10.1016/j.engstruct.2022.114381.
[5] I.N. Psycharis, I.M. Kalyviotis, H.P. Mouzakis, Experimental investigation of the response of precast concrete cladding panels with integrated connections under monotonic and cyclic loading, Eng Struct 159 (2018) 75–88. https://doi.org/10.1016/j.engstruct.2017.12.036.
[6] A. Furtado, R. Sousa, R. Carmo, E. Júlio, Desafios na simulação numérica de construções modulares pre-fabricadas em betão armado. In Proceedings of the 13º Congresso Nacional de Sismologia e Engenharia Sísmica, Sísmica 2024, Guimaraes, Portugal, 17–19 April 2024.
[7] G. Resta, S. Gonçalves, Design for disassembly and cultural sites. The use of modular architecture and prefabrication in exhibition venues, VITRUVIO - International Journal of Architectural Technology and Sustainability 9 (2024) 78–95. https://doi.org/10.4995/vitruvio-ijats.2024.21442.
[8] Abaqus, (2017).
[9] “European Committee for Standardization” CEN, EN 1992-1-1 Eurocode 2: Design of concrete structures - Part 1-1 : General rules and rules for buildings, (2004).
[10] A.S. Genikomsou, M.A. Polak, Finite element analysis of punching shear of concrete slabs using damaged plasticity model in ABAQUS, Eng Struct 98 (2015) 38–48. https://doi.org/10.1016/j.engstruct.2015.04.016.
[11] CEB-FIP, CEB FIP model code 1990, (1990) 462.